Nucleation of Iron Oxide Nanoparticles Mediated by Mms6 Protein *in Situ*

Sanjay Kashyap,[†] Taylor J. Woehl,[†] Xunpei Liu,[‡] Surya K. Mallapragada,[†,‡] and Tanya Prozorov[†,*]

[†]Ames Laboratory, U.S. Department of Energy, Ames, Iowa 50011, United States, and [‡]Department of Chemical and Biological Engineering, Iowa State University, Ames, Iowa 50011, United States

ABSTRACT

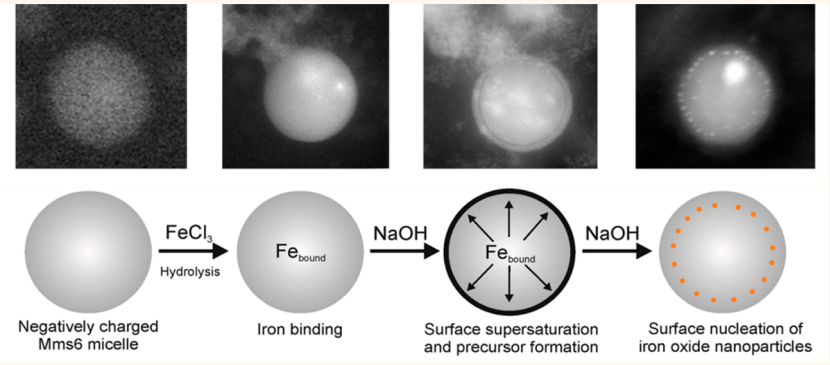

Biomineralization proteins are widely used as templating agents in biomimetic synthesis of a variety of organic—inorganic nanostructures. However, the role of the protein in controlling the nucleation and growth of biomimetic particles is not well understood, because the mechanism of the bioinspired reaction is often deduced from *ex situ* analysis of the resultant nanoscale mineral phase. Here we report the direct visualization of biomimetic iron oxide nanoparticle nucleation mediated by an acidic bacterial recombinant protein, Mms6, during an *in situ* reaction induced by the controlled addition of sodium hydroxide to solution-phase Mms6 protein micelles incubated with ferric chloride. Using *in situ* liquid cell scanning transmission electron microscopy we observe the liquid iron prenucleation phase and nascent amorphous nanoparticles forming preferentially on the surface of protein micelles. Our results provide insight into the early steps of protein-mediated biomimetic nucleation of iron oxide and point to the importance of an extended protein surface during nanoparticle formation.

KEYWORDS: recombinant iron-binding protein · protein-mediated particle nucleation · *in situ* TEM analysis

In biological systems, proteins and other biological macromolecules play an important role in controlling the size and shape of biogenic material *via* direct interactions with certain mineral faces. Self-assembly of polar and charged residues of biomacromolecules is thought to regulate their interactions with the atomic array of certain crystal planes on the mineral surface.[1−5] These direct interactions are assumed to provide a close coordination with certain facets of the mineral phase, thereby facilitating growth of certain crystal faces and inhibiting growth of others.[5−13]

Protein-driven nucleation is believed to play an important role in the formation and growth of both biogenic and biomimetic nanocrystals.[11,14−17] One of the best-studied biomineralization systems is calcium carbonate, where the directed growth is reportedly determined at the initial stage of nucleation *via* specific interaction of nuclei with the functional groups of the organic interface, leading to formation of a specific inorganic phase.[18−22] The nascent inorganic phase is affected by the site-adsorbed cation structure, with the shape and morphology of the crystal influenced by the amorphous-like precursor phase.[23−29] Multiple studies suggest that the nucleation of metallic particles on a biomacromolecular template is initiated by the adsorption of cations or cation complexes onto the negatively charged surface sites *via* simple electrostatic interactions.[30,31] In the biomimetic calcium phosphate system, for example, prenucleation clusters were recently identified as ion-associated complexes, with charged protein aggregates taking up large amounts of positively charged calcium ions and facilitating the nanoparticle nucleation.[32]

* Address correspondence to tprozoro@ameslab.gov.

Received for review May 9, 2014 and accepted August 27, 2014.

Published online August 27, 2014
10.1021/nn502551y

There is a considerable interest in biomimetic fabrication of functional magnetic nanostructures in the presence of synthetic polymers, viruses, peptides, DNA molecules, proteins, and various polymer-based hybrid materials employed as matrices, scaffolds, and templating agents.[8,14,33−44] Bioinspired synthesis of magnetite nanocrystals can be carried out *in vitro* utilizing proteins from magnetotactic bacteria.[45−49] Magnetotactic bacteria are a diverse family of aquatic prokaryotes known to biomineralize intracellular membrane-bound crystals of magnetic nanocrystals called magnetosomes, typically magnetite (Fe_3O_4) or greigite (Fe_3S_4).[50−53] Among the several acidic membrane proteins tightly bound to the magnetosome magnetite crystal, Mms6 is believed to be one of the dominant proteins involved in magnetosome formation and growth.[54,55] The full-length recombinant acidic protein *His*-Mms6 was shown to promote the shape-specific formation of magnetic nanocrystals *in vitro*.[45,46,49,55−58] This biomimetic approach was later utilized in the templated synthesis of more complex and highly magnetic cobalt ferrite nanocrystals in the presence of the functional acidic C-terminus (*i.e.*, carboxylate-terminated region) of Mms6.[57,59,60] The nominal molecular mass of Mms6 is 10.2 kDa; however, in aqueous solutions this protein is not present as a monomer. Instead, Mms6 undergoes spontaneous self-assembly and forms micelles with significantly higher apparent molecular mass, typically consisting of 20−40 protein molecules.[44,61,62] Both full-length *His*-Mms6 and its C-terminus were shown to be amphiphilic and to multimerize and form micelles in solution, with the iron binding presumably taking place at the hydrophilic C-termini of the Mms6.[44,61,62] However, neither the macromolecular structures nor the localization of the bound iron to the micelle surface has been established so far. In the biomimetic synthesis of cobalt ferrite in the presence of the synthetic C-terminus of Mms6, the protein was reported to control the size, shape, and phase of cobalt ferrite nanoparticles by changing the kinetics of the nucleation and growth process *via* uniform catalytic oxidation of the nuclei.[56,59] The classical model of nucleation is not applicable for this system, as the thermodynamics and kinetics of nucleation are reportedly altered by the biomacromolecule.[59] MamC is another magnetosome membrane protein present in several strains of magnetotactic bacteria.[58,63−66] Similar to Mms6, MamC is amphiphilic, with a hydrophilic C-terminus assumed to play an active role in magnetite biomineralization.[64,66] Self-assembly of MamC into negatively charged macromolecular complexes and iron binding to their surface have been recently reported.[67]

For the majority of bioinspired systems the mechanism of nanoparticle formation remains unclear, because the analysis of the nanomaterial growth is either performed by taking sample aliquots during different stages of the growth process or carried out *after* the synthesis.[46,59,60,68−74] This approach provides important clues relevant to the overall effect of the templating agent, permits characterization of a *resultant biomimetic material,* and allows an indirect inference of the nanoparticle growth pathway. However, it generally lacks information about the *dynamics of the material's formation*.[59,60,75−77] As a result, despite numerous reports on mineral−protein interactions and iron biomineralization processes, the fundamental templating interactions and nucleation and growth processes are not well understood. In order to obtain reliable information on fundamental dynamic functions or processes involved in protein-templated biomineralization, it is imperative to study the biological and biomacromolecular systems in their native, fully hydrated environments, rather than as altered "prepared" samples, which are prone to artifacts. Use of fluid cell transmission electron microscopy (TEM) has allowed real-time imaging of intact biological structures in their native liquid environment with sufficiently high spatial and temporal resolution, enabling visualization of many dynamic physical, chemical, and structural nanoscale phenomena taking place in liquids.[76,78−89] While imaging low-contrast organic materials is notoriously difficult with TEM, a number of recent fluid cell TEM and scanning TEM (STEM) studies have elucidated the mechanisms of dynamic processes in soft nanomaterials and biomacromolecules.[83,85,87,90,91] Notably, Parent and co-workers demonstrated that palladium nanoparticle growth in a block copolymer micellar template proceeds by monomer addition followed by aggregation and coalescence, knowledge that was used to engineer optimized mesoporous nanoparticles with ordered pores.[87,91] The motion of platinum-loaded micellar nanoparticles in liquid has been observed using *in situ* liquid cell TEM, indicating that this technique is uniquely suited for imaging dynamics of soft nanomaterials.[92]

Here we report the direct visualization of iron binding of the self-assembled bacterial recombinant acidic biomineralization protein Mms6 in the solution phase and subsequent protein-directed nanoparticle nucleation *in situ*. A well-characterized mammalian iron storage protein, ferritin, previously visualized with the *in situ* fluid cell TEM, was used as a reference.[83] Our results provide important insights into the specific surface interactions of self-assembled protein micelles with metal ions and their role in biomimetic iron oxide nanoparticle nucleation. Our findings are applicable for *in situ* characterization of a variety of dynamic processes taking place at inorganic−organic interfaces in protein solutions and for optimization of synthetic conditions in a variety of bioinspired reactions.

RESULTS AND DISCUSSION

The macromolecules have higher mass density and average atomic number compared to the surrounding buffer solution and can be visualized with various

TEM techniques. We performed cryo-TEM and HAADF-STEM imaging to characterize the structure and chemistry of the Mms6 micelles *ex situ*. Figure 1 shows a cryo-TEM image of vitrified Mms6 micelles (Figure 1a) accompanied by a HAADF-STEM image of micelles dried on a carbon grid for comparison (Figure 1b). The proteinaceous micelles are clearly visible as spherical structures in the vitrified and dried sample, where both sample preparations reveal the micelles to have average sizes of 25−150 nm. The micelles appear aggregated in the dried sample, which is likely an artifact created by capillary drying forces. This aggregation further reinforces the need to perform *in situ* imaging of the protein complexes in order to characterize them in their native hydrated state.

To ensure specimen stability, minimize its thickness, and provide an adequate signal for electron energy loss spectroscopy (EELS) and energy-filtered TEM (EFTEM), additional characterization was conducted on ferric chloride incubated Mms6 prepared on a conventional EM grid. Figure 2 shows EFTEM elemental maps of the Fe $L_{2,3}$-edge (b) and O K-edge (c) energy loss values, in addition to the corresponding zero-loss image (a). The EFTEM elemental maps confirm the presence of oxygen and iron in Mms6 proteinaceous micelles incubated with ferric chloride. Although the iron peaks are significantly weaker compared to that of oxygen (due to the higher energy loss and lower signal-to-noise ratio of the Fe $L_{2,3}$-edge), the elements are clearly distinguishable. Figures 2d,e show the corresponding oxygen and iron EELS spectra collected from a single micelle, respectively.

Figure 3 shows *in situ* liquid cell HAADF-STEM images of Mms6 proteinaceous micelles suspended in buffer solution. The hydrated micelles in buffer solution appear as spherical structures with higher contrast due to an increased mass density compared to the surrounding solution (Figure 3a). The size of the hydrated micelles is similar to that of the vitrified and dried micelles shown in Figure 1. While the image contrast and signal-to-noise are markedly lower than those of the micelles on a grid (*cf.* Figure 1b), the *in situ* image indicates that HAADF-STEM imaging of these low atomic number micelles in liquid is possible, even though previous works utilized TEM imaging and/or heavy metal loading to image synthetic micelles and biomacromolecules in liquid.[83,92] After initial imaging of the Mms6 micelles, dilute ferric chloride solution was delivered to the fluid cell *via* fluid flow channels *in situ*. The proteinaceous micelles were allowed to incubate with the ferric chloride for 60 min and then subsequently washed with water delivered *in situ*. The exposure to ferric chloride solution *in situ* did not induce significant changes in the size of the proteinaceous micelles, as illustrated by the before and after HAADF-STEM images and size distributions in Figure S1

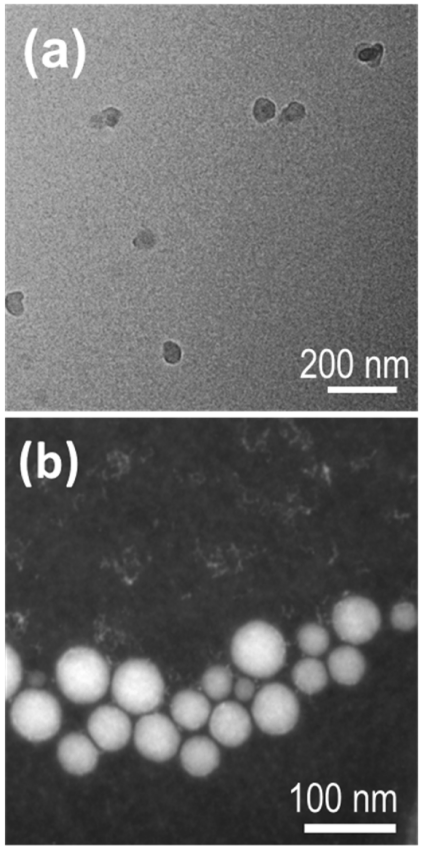

Figure 1. *Ex situ* images of micelles of the biomineralization recombinant protein Mms6: (a) Cryo-TEM image of vitrified micelles, scale bar 200 nm. (b) HAADF-STEM image of micelles dried on a grid.

shown in the Supporting Information. A relatively low image contrast likely led to some error in the size measurements, thus contributing to a larger size distribution. The incubation of the protein micelles with ferric chloride *in situ* led to a noticeable enhancement in the Z-contrast of the protein micelles (Figure 1c), attributed to binding and subsequent surface localization of iron. Because the size and shape of the Mms6 micelles did not change after iron incubation (Figure S1), we assume the contrast change was due solely to the presence of the higher atomic number iron species in the micelles.

The addition of NaOH *in situ* induces local pH gradients and affects the formed hydrolyzed species, as exemplified in Figure 4. Before NaOH is added to induce iron oxide nucleation, the Mms6 micelles have relatively constant Z-contrast from the center to edge, indicating a relatively constant concentration of iron species throughout (Figure 4a). The proteinaceous micelles appeared stable under the current imaging conditions, exhibiting no electron beam damage. Moreover, no reduction of ferric iron caused by the electron beam could be detected prior to the delivery of NaOH *in situ*. On the basis of this observation, it was concluded that under our experimental conditions aqueous ferric iron is not readily reduced by the

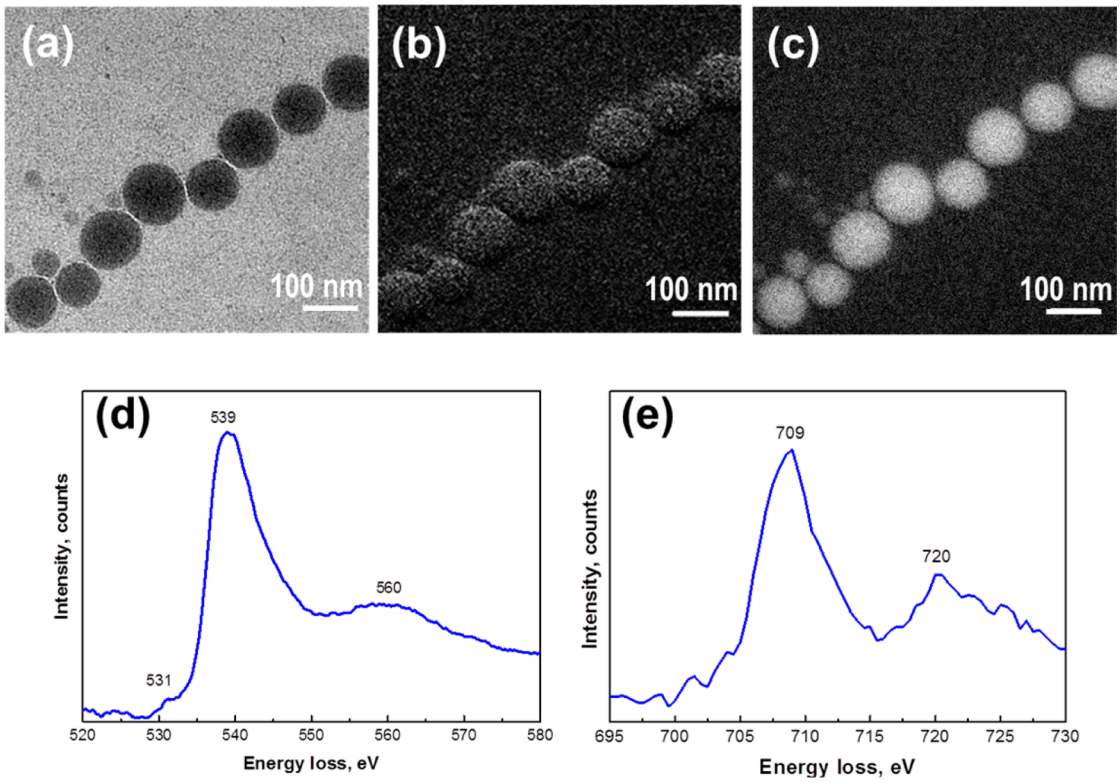

Figure 2. *Ex situ* **EFTEM and EELS analysis of Mms6 micelles. Zero-loss image (a) and elemental maps of (b) iron and (c) oxygen acquired in EFTEM mode from Mms6 incubated with ferric chloride, from a specimen prepared on a grid. Scale bar: 200 nm. (d, e) EELS spectra acquired from the specimen at the oxygen and iron edges, respectively.**

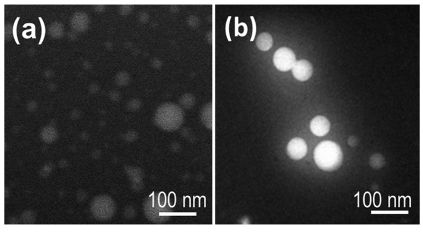

Figure 3. *In situ* **fluid cell HAADF-STEM images of Mms6 micelles in buffer (a) before and (b) after incubation with ferric chloride.**

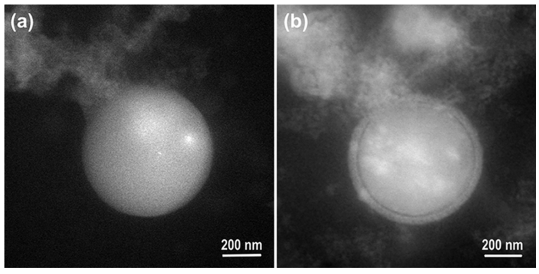

Figure 4. *In situ* **fluid cell HAADF-STEM images of Mms6 micelles in buffer during reaction with NaOH. (a) Iron-incubated Mms6 micelle before addition of NaOH. (b) Same micelle after initial addition of NaOH, showing contrast change due to possible formation of an amorphous iron-rich precursor surface layer. Scale bar: 200 nm.**

electron beam, and e-beam-induced nucleation on the micellar surfaces can be ruled out.[93,94]

Hydrolysis of Fe(III) salt solutions in bulk media can lead to a variety of structures, with the key factors in the formation and crystallinity of formed iron oxides being the concentration of Fe(III), rate at which the hydrolyzed species are supplied to the growing crystal, pH, and temperature.[95−98] The formation of ferrihydrite is favored when the rate of supply of growth units is relatively rapid, resulting in formation of poorly crystalline particulates, while the formation of green rust in the case of ferric chloride, without the ferrous iron, is unlikely.[97] The presence of a negatively charged micellar surface and high concentration of surface-bound ferric iron apparently lower the energy barrier to subsequent nucleation, thus facilitating this process. At higher OH/Fe ratios, the growth units are supplied more slowly, permitting the controlled ordering needed for formation of better-shaped particles.[95,97,99] As the pH increases during the *in situ* delivery of NaOH solution, the variation of localized iron concentration and supply of reagents to the growing crystal govern the nucleation by affecting the nominal OH/Fe ratio.[95,97]

After NaOH is added, a lower contrast "halo" forms around the perimeter of the micelle, which can be attributed, in part, to surface depletion of the higher atomic number bound iron. We propose that this is likely the first step in the formation of a liquid-like, disordered prenucleation phase (Figure 4b), followed by the subsequent nucleation of iron oxide nanoparticles.

Alternatively, a change in micellar surface association of protein induced by the pH alteration could lead to an instantaneous change in protein dissociation and prompt a temporary release of protein–iron complexes into the surrounding solution. This would lead to formation of transient iron-associated protein entities, likely manifested as a halo. It is worth noting that visualization of this highly dynamic process was made possible only by *in situ* fluid cell STEM imaging and currently could not be validated by other experimental techniques. Self-assembly of protein into micelles and emergence of the resultant micellar surface-bound iron appear to play a crucial role in biomimetic particle development by sustaining the ferric ion delivery to the forming amorphous prenucleation phase and lowering the energy barrier to subsequent nucleation. The protein-directed iron surface concentration, therefore, affects the rate of formation of biomimetic iron oxide nanoparticles. The Mms6 presently is not available in its monomeric form; however, we hypothesize that in the absence of a micellar surface the amorphous precursor would not form locally.

Mms6 binds Fe^{3+} and increases the local iron concentration in specific negatively charged areas favoring the nucleation of a disordered precursor phase, likely (2-line-) ferrihydrite, often called "hydrous ferric oxide", or "amorphous iron oxide", which is believed to be the first step in biomimetic formation of magnetite.[49,55,56,61,100] Following the surface depletion of prenucleation liquid iron-rich complex (*cf.* Figure 4b), iron oxide nuclei begin to form preferentially on the surface of the Mms6 micelles (Figure 5a), although at this point particle nucleation in the interior region of the micelles cannot be excluded. Iron oxide nanoparticles are not observed to undergo aggregation during nucleation; they appear and grow independently. The notable lack of spontaneous *bulk* nucleation (outside the micelles) suggests that the high iron concentration near the micellar surface likely leads to supersaturation conditions necessary for localized nucleation. Preferential iron–protein surface binding leads to a removal of ferric ions from the bulk solution, essentially leading to a surface-localized supersaturation of the prenucleation iron-rich ion complex with respect to the nucleating amorphous nanoparticles. Surface-localized iron binding has also been recently observed using *in situ* liquid cell STEM for the recombinant membrane protein MamC.[67]

Our direct observations of iron binding and micelle-localized nucleation are consistent with our previous studies that have shown the hydrophilic C-terminal region of Mms6, which is present at the corona of the micelles, is the active site of the protein for iron binding and biomineralization.[56,61,62] Importantly, our direct observations of micelle-localized iron oxide nucleation reinforce the idea that the presence of Mms6 protein in bacterial magnetosome membrane vesicles could, arguably, lead to localization of iron on the magnetosome membrane surface, facilitating and directing the shape-specific magnetite biomineralization by the magnetotactic bacteria.

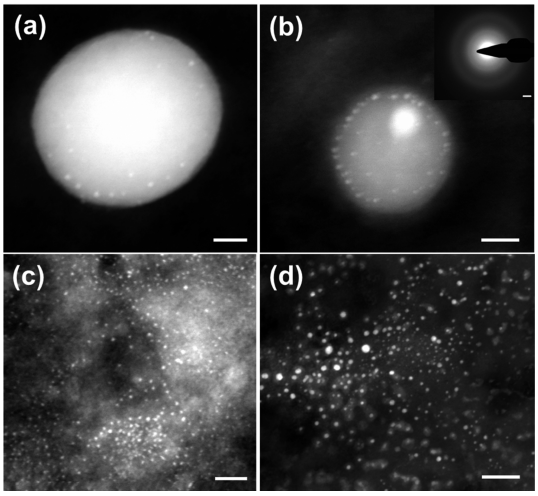

Figure 5. HAADF-STEM images acquired after reaction of ferric chloride with NaOH: (a) Mms6 micelles in the fluid cell holder *in situ*; (b) Mms6 micelles on an EM grid *ex situ*. The inset shows the corresponding selected area electron diffraction pattern. Inset scale bar: 2 1/nm. (c) In the absence of Mms6 *ex situ* on an EM grid, and (d) in the absence of Mms6 *in situ*. Scale bar: 20 nm.

Similar to the *in situ* reaction with NaOH, analysis of iron oxide nucleation on protein-bearing EM grids exposed to NaOH *ex situ* revealed preferential nucleation on the surface of proteinaceous micelles as well (Figure 5b). HAADF-STEM images of the biomimetic nuclei performed *ex situ* shows formation of disordered particles with an average size of 1.2 nm. On the basis of the analysis of electron diffraction patterns (Figure 5b), the nascent nuclei could be best identified as amorphous iron oxide, in good agreement with the proposed formation of disordered ferrihydrite. In comparison, *ex situ* exposure of ferric chloride to NaOH without the Mms6 resulted in a random formation of a large number of nuclei (Figure 5c). Therefore, nucleation of iron oxide in the presence of Mms6 provides a unique synthetic pathway for localized growth at the micellar surface. In control *in situ* fluid cell experiments without Mms6, nanoparticles were also found to nucleate randomly (Figure 5d). As we observed no aggregation during *in situ* nucleation in the presence of protein micelles, the Mms6 protein-mediated synthesis might aid in preventing uncontrolled aggregation of iron oxide nanoparticles, promoting uniform nucleation and affecting subsequent growth.

The schematic in Figure 6 summarizes the proposed mechanism for Mms6 micelle-mediated iron oxide nucleation and growth. Initially negatively charged Mms6 micelles are present in solution with sizes ranging from 25 to 150 nm (a). Ferric chloride is added to the solution, and the negatively charged micelle surface binds Fe(III) with minimal change to

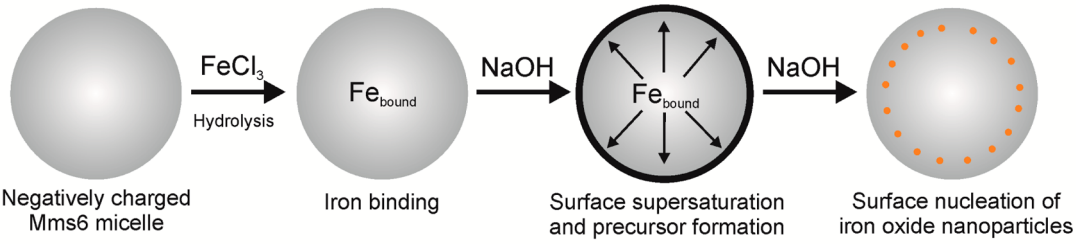

Figure 6. Schematic of Mms6-mediated iron oxide nucleation of micelle-bound iron species.

their shape and size, with ferric iron species concentrating at the surface of the Mms6. Upon controlled addition of NaOH, the change in pH leads to formation of an amorphous iron-rich prenucleation complex, resulting in surface-localized supersaturation with respect to a disordered solid phase, likely ferrihydrite. It is worth noting, however, that detailed phase analysis of the nascent nucleation phase is currently impractical because of its amorphous nature. Binding of Fe(III) by the Mms6 micelles minimizes uncontrolled nucleation of iron oxide in the bulk solution. Upon further increase of pH, the conditions become conducive for nucleation of first iron oxide nanoparticles, which are observed to form preferentially at the micellar surface during the controlled reaction with NaOH. Nucleation of iron oxide particulates occurs relatively free from interparticle interactions, such as aggregation, due to the templating action of the protein micelle.

CONCLUSIONS

In summary, we have visualized iron binding of the self-assembled bacterial recombinant acidic Mms6 protein by utilizing *in situ* liquid cell HAADF-STEM imaging. The micelles are visible without heavy-metal loading, indicating that *in situ* liquid cell HAADF-STEM imaging is a viable technique for observing organic micelles in liquid. Upon incubation in ferric chloride, the Z-contrast of the micelles is further increased due to iron binding. Slow addition of NaOH to the micelles *in situ* leads to a contrast change at the surface of the micelles, which we attribute to the formation of an amorphous precursor phase. Further addition of NaOH led to nucleation of iron oxide on the micelles. No aggregation was observed during nucleation, and nucleation was not observed to occur in the bulk outside of the micelles. These results suggest that protein self-assembly and micellar surface iron binding lower the energy barrier to subsequent nucleation, thus facilitating this process. Our findings are applicable for optimization of bioinspired synthesis of magnetic nanoparticles. Our results provide, for the first time, direct evidence of the localization of the bound iron to the C-terminal region of the Mms6 micelles and improve the current understanding of the relationship between the self-organization of recombinant acidic proteins, surface-localized metal binding, and formation of a macromolecule–solution interface, critical for protein-assisted nucleation of biomimetic magnetic nanoparticles.

METHODS

Materials and Reagents. Ferritin (CalBiochem) and Mms6 used in the study were dialyzed against an identical buffer (20 mM TRIS, 100 mM KCl, pH 7.45). All aqueous solutions were prepared with deionized water passed through a Millipore Milli-Q Plus water purification system ($\lambda = 18.2$ MΩ) and sparged with argon for 15 min. Ferric chloride hexahydrate ($FeCl_3 \cdot 6H_2O$, >99%) was purchased from Sigma-Aldrich and used without purification. The molecular mass of Mms6 is 10.2 kDa, however in aqueous solution forms Mms6 micelles.[61,62,101] The amount of protein in solution was maintained at 0.67 μM; Mms6 was incubated with 10 μM ferric chloride solution prepared from a deoxygenated 0.5 M stock solution.

Specimen Preparation. To minimize the thickness of the liquid layer, the protein solutions were deposited with a Nano eNabler molecular printer (BioForce Sciences) onto plasma-cleaned electron-transparent silicon nitride window membranes for *in situ* imaging and carbon-coated Au grids (QuantiFoil) for *ex situ* imaging. The molecular printer permitted the deposition of extremely small amounts of liquid (femptoliters).[102,103] Silicon nitride window membranes were cleaned by rinsing in toluene (3 × 3 mL), rinsed with chemically pure acetone (3 × 3 mL), and washed with ethanol (3 × 5 mL), followed by cleaning in ozone plasma cleaner (BioForce) for 45 min. Immediately after the plasma cleaning, the window membranes were functionalized with (3-aminopropyl)triethoxysilane (APTES) to facilitate the protein surface immobilization.[67,104,105] To ensure protein integrity during the specimen deposition, silicon nitride windows were loaded on a custom-made cold stage at 7 °C, while maintaining the appropriate humidity levels.[67]

Dynamic Light Scattering. Dynamic light scattering (DLS) and measurements of zeta potentials of the protein solutions were carried out with a Zetasizer nanoparticle analyzer (model: ZEN3690, Malvern Instrument Ltd., Southborough, MA, USA). Prior to analysis, the buffer was filtered through a 0.2 μm nitrocellulose membrane and the protein specimens were centrifuged for 20 min (1000 rpm, 23 °C). The particle size distributions were acquired on numerous 10 s acquisitions with three repeats. Data were processed using Dispersion Technology Software 5.00 (Malvern Instrument Ltd.).

***In Situ* Fluid Cell Characterization.** The iron-binding proteins were examined with a continuous flow fluid cell TEM holder platform (Hummingbird Scientific). After the membrane functionalization and protein deposition, the windows were assembled and sealed in the liquid cell holder platform, resulting in the liquid specimen being sandwiched between the electron-transparent silicon nitride window membranes. Imaging and characterization of the specimens were carried out

with an FEI Tecnai G^2 F20 (S)TEM operating at an accelerating voltage of 200 kV equipped with a Tridiem Gatan imaging filter, high angle annular dark field, and energy-dispersive X-ray spectroscopy detectors. *In situ* fluid delivery was carried out with a syringe pump with a variable pumping speed (2−5 μL/min). For comparison, specimens were also printed on conventional EM grids and examined with a standard single-tilt holder. Electron energy loss spectroscopy was used to probe the localized chemical composition of the liquid specimens. Elemental maps of oxygen and iron were acquired in energy-filtered transmission electron microscopy mode with a slit width 30 $\pm$ 1 eV. EELS spectra were acquired with a slit width of 10 eV and dispersion of 0.5 eV/pixel. Data analysis was performed with Digital Micrograph software (GMS version 2.11.1404.0) and OriginPro 9.0 software. To ensure reproducibility of results, micelle sizes were measured on micelles imaged in numerous micrographs obtained in the HAADF-STEM mode.

Conflict of Interest: The authors declare no competing financial interest.

Supporting Information Available: Supporting images, protein micelle size distributions, dynamic light scattering, and ferritin images and spectra. This material is available free of charge *via* the Internet at http://pubs.acs.org.

Acknowledgment. T.P. acknowledges support from the Department of Energy, Office of Science, Early Career Research Award, Biomolecular Materials Program. This work was supported by the U.S. Department of Energy, Office of Basic Energy Science, Division of Materials Sciences and Engineering. The research was performed at the Ames Laboratory, which is operated for the U.S. Department of Energy by Iowa State University under Contract No. DE-AC02-07CH11358. The authors thank Prof. Marit Nilsen-Hamilton and her laboratory for providing the recombinant biomineralization protein Mms6.

REFERENCES AND NOTES

1. Politi, Y.; Metzler, R. A.; Abrecht, M.; Gilbert, B.; Wilt, F. H.; Sagi, I.; Addadi, L.; Weiner, S.; Gilbert, P. Transformation Mechanism of Amorphous Calcium Carbonate into Calcite in the Sea Urchin Larval Spicule. *Proc. Natl. Acad. Sci. U.S.A.* **2008**, *105*, 17362–17366.
2. Gordon, L. M.; Joester, D. Nanoscale Chemical Tomography of Buried Organic-Inorganic Interfaces in the Chiton Tooth. *Nature* **2011**, *469*, 194–197.
3. Belcher, A.; Wu, X.; Christensen, R.; Hansma, P.; Stucky, G.; Morse, D. Control of Crystal Phase Switching and Orientation by Soluble Mollusc-Shell Proteins. *Nature* **1996**, *381*, 56–58.
4. Falini, G.; Albeck, S.; Weiner, S.; Addadi, L. Control of Aragonite or Calcite Polymorphism by Mollusk Shell Macromolecules. *Science* **1996**, *271*, 67–69.
5. Addadi, L.; Weiner, S. Biomineralization: Crystals, Asymmetry and Life. *Nature* **2001**, *411*, 753–755.
6. Addadi, L.; Weiner, S.; Geva, M. On How Proteins Interact with Crystals and Their Effect on Crystal Formation. *Z. Kardiol.* **2001**, *90*, iii/92–iii/98.
7. Aizenberg, J.; Weaver, J. C.; Thanawala, M. S.; Sundar, V. C.; Morse, D. E.; Fratzl, P. Skeleton of Euplectella sp.: Structural Hierarchy from the Nanoscale to the Macroscale. *Science* **2005**, *309*, 275–278.
8. Bhushan, B. Biomimetics: Lessons From Nature - an Overview. *Philos. Trans. R. Soc. A* **2009**, *367*, 1445–1486.
9. Gao, H.; Ji, B.; Jäger, I. L.; Arzt, E.; Fratzl, P. Materials Become Insensitive to Flaws at Nanoscale: Lessons from Nature. *Proc. Natl. Acad. Sci.* **2003**, *100*, 5597–5600.
10. Kamat, S.; Su, X.; Ballarini, R.; Heuer, A. H. Structural Basis for the Fracture Toughness of the Shell of the Conch Strombus Gigas. *Nature* **2000**, *405*, 1036–1040.
11. Archibald, D. D.; Mann, S. Template Mineralization of Aelf-Assembled Anisotropic Lipid Microstructures. *Nature* **1993**, *364*, 430–433.
12. Mann, S.; Meldrum, F. C. Controlled Synthesis of Inorganic Materials Using Supramolecular Assemblies. *Adv. Mater.* **1991**, *3*, 316–318.
13. Mann, S. *Biomineralization: Principles and Concepts in Bioinorganic Materials Chemistry*; Oxford University Press: USA, 2001.
14. Reichhardt, C.; Uchida, M.; O'Neil, A.; Li, R.; Prevelige, P. E.; Douglas, T. Templated Assembly of Organic-Inorganic Materials Using the Core Shell Structure of the P22 Bacteriophage. *Chem. Commun.* **2011**, *47*, 6326–6328.
15. Lee, N.; Kim, H.; Choi, S. H.; Park, M.; Kim, D.; Kim, H.-C.; Choi, Y.; Lin, S.; Kim, B. H.; Jung, H. S.; *et al*. Magnetosome-Like Ferrimagnetic Iron Oxide Nanocubes for Highly Sensitive MRI of Single Cells and Transplanted Pancreatic Islets. *Proc. Natl. Acad. Sci.* **2007**, *108*, 2662–2667.
16. Wang, B.; Liu, P.; Jiang, W.; Pan, H.; Xu, X.; Tang, R. Yeast Cells with an Artificial Mineral Shell: Protection and Modification of Living Cells by Biomimetic Mineralization. *Angew. Chem., Int. Ed.* **2008**, *47*, 3560–3564.
17. Chang, Y.-S.; Savitha, S.; Sadhasivam, S.; Hsu, C.-K.; Lin, F.-H. Fabrication, Characterization, and Application of Greigite Nanoparticles for Cancer Hyperthermia. *J. Colloid Interface Sci.* **2011**, *363*, 314–319.
18. Aizenberg, J.; Black, A. J.; Whitesides, G. M. Oriented Growth of Calcite Controlled by Self-Assembled Monolayers of Functionalized Alkanethiols Supported on Gold and Silver. *J. Am. Chem. Soc.* **1999**, *121*, 4500–4509.
19. Travaille, A. M.; Donners, J. J. J. M.; Gerritsen, J. W.; Sommerdijk, N. A. J. M.; Nolte, R. J. M.; Van Kempen, H. Aligned Growth of Calcite Crystals on a Aelf-Assembled Monolayer. *Adv. Mater.* **2002**, *14*, 492–495.
20. Travaille, A. M.; Kaptijn, L.; Verwer, P.; Hulsken, B.; Elemans Johannes, A. A. W.; Nolte Roeland, J. M.; van Kempen, H. Highly Oriented Self-Assembled Monolayers as Templates for Epitaxial Calcite Growth. *J. Am. Chem. Soc.* **2003**, *125*, 11571–11577.
21. Hugli, R. V.; Duff, G.; O'Conchuir, B.; Mengotti, E.; Rodriguez, A. F.; Nolting, F.; Heyderman, L. J.; Braun, H. B. Artificial Kagome Spin Ice: Dimensional Reduction, Avalanche Control and Emergent Magnetic Monopoles. *Philos. Trans. R. Soc. A* **2012**, *370*, 5767–5782.
22. Nielsen, M. H.; Lee, J. R. I.; Hu, Q.; Han, T. Y.-J.; De Yoreo, J. J. Structural Evolution, Formation Pathways and Energetic Controls during Template-Directed Nucleation of $CaCO_3$. *Faraday Discuss.* **2012**, *159*, 105–121.
23. De Yoreo, J. J.; Vekilov, P. G. Principles of Crystal Nucleation and Growth. *Rev. Mineral. Geochem.* **2003**, *54*, 57–93.
24. De Yoreo, J. J.; Dove, P. M. Materials Science: Shaping Crystals with Biomolecules. *Science* **2004**, *306*, 1301–1302.
25. Vekilov, P. G.; Galkin, O.; Shchukin, E. D. Fundamental Aspects of Nucleation Theory Revealed in Experiments with Protein Solid Phases. *Str. Assembl. Solid Fluid Interface* **2004**, *2*, 105–144.
26. de Yoreo, J. J.; Wierzbicki, A.; Dove, P. M. New Insights Into Mechanisms of Biomolecular Control on Growth of Inorganic Crystals. *CrystEngComm* **2007**, *9*, 1144–1152.
27. Tamerler, C.; Sarikaya, M. Molecular Biomimetics: Nanotechnology and Bionanotechnology Using Genetically Engineered Peptides. *Philos. Trans. R. Soc. A* **2009**, *367*, 1705–1726.
28. Dey, A.; Bomans, P. H. H.; Mueller, F. A.; Will, J.; Frederik, P. M.; de With, G.; Sommerdijk, N. A. J. M. The Role of Prenucleation Clusters in Surface-Induced Calcium Phosphate Crystallization. *Nat. Mater.* **2010**, *9*, 1010–1014.
29. Whitelam, S. Control of Pathways and Yields of Protein Crystallization through the Interplay of Nonspecific and Specific Attractions. *Phys. Rev. Lett.* **2010**, *105*, 088102/1–088102/4.
30. Tarasevich, B. J.; Rieke, P. C.; McVay, G. L.; Fryxell, G. E.; Campbell, A. A. Synthesis of Ceramic Ultrastructures Utilizing Biological Processes. *Chem. Process. Adv. Mater.* **1992**, 529–542.
31. Malone, S. A.; Lewin, A.; Kilic Mehmet, A.; Svistunenko Dimitri, A.; Cooper Chris, E.; Wilson Michael, T.; Le Brun Nick, E.; Spiro, S.; Moore Geoffrey, R. Protein-Template-Driven Formation of Polynuclear Iron Species. *J. Am. Chem. Soc.* **2004**, *126*, 496–504.

32. Habraken, W. J. E. M.; Tao, J.; Brylka, L. J.; Friedrich, H.; Bertinetti, L.; Schenk, A. S.; Verch, A.; Dmitrovic, V.; Bomans, P. H. H.; Frederik, P. M.; *et al.* Ion-Association Complexes Unite Classical and Non-Classical Theories for the Biomimetic Nucleation of Calcium Phosphate. *Nat. Commun.* **2013**, *4*, 1507.
33. Allen, M.; Willits, D.; Young, M.; Douglas, T. Constrained Synthesis of Cobalt Oxide Nanomaterials in the 12-Subunit Protein Cage from Listeria innocua. *Inorg. Chem.* **2003**, *42*, 6300–6305.
34. Douglas, T.; Stark, V. T. Nanophase Cobalt Oxyhydroxide Mineral Synthesized within the Protein Cage of Ferritin. *Inorg. Chem.* **2000**, *39*, 1828–1830.
35. Klem, M. T.; Young, M.; Douglas, T. Biomimetic Magnetic Nanoparticles. *Mater. Today* **2005**, *8*, 28–37.
36. Reiss, B. D.; Mao, C.; Solis, D. J.; Ryan, K. S.; Thomson, T.; Belcher, A. M. Biological Routes to Metal Alloy Ferromagnetic Nanostructures. *Nano Lett.* **2004**, *4*, 1127–1132.
37. Meldrum, F. C.; Heywood, B. R.; Mann, S. Magnetoferritin: *In Vitro* Synthesis of a Novel Magnetic Protein. *Science* **1992**, *257*, 522–523.
38. Sano, K.-I.; Ajima, K.; Iwahori, K.; Yudasaka, M.; Iijima, S.; Yamashita, I.; Shiba, K. Endowing a Ferritin-Like Cage Protein with High Affinity and Selectivity for Certain Inorganic Materials. *Small* **2005**, *1*, 826–832.
39. Tartaj, P.; del Puerto Morales, M.; Veintemillas-Verdaguer, S.; Gonzalez-Carreno, T.; Serna, C. J. The Preparation of Magnetic Nanoparticles for Applications in Biomedicine. *J. Phys. D: Appl. Phys.* **2003**, *36*, R182–R197.
40. Resnick, D.; Gilmore, K.; Idzerda, Y. U.; Klem, M.; Smith, E.; Douglas, T. Modeling of the Magnetic Behavior of g-Fe_2O_3 Nanoparticles Mineralized in Ferritin. *J. Appl. Phys.* **2004**, *95*, 7127–7129.
41. Grunwald, I.; Rischka, K.; Kast, S. M.; Scheibel, T.; Bargel, H. Mimicking Biopolymers on a Molecular Scale: Nano-(bio)technology Based on Engineered Proteins. *Philos. Trans. R. Soc. A* **2009**, *367*, 1727–1747.
42. Nardin, C.; Meier, W. Hybrid Materials from Amphiphilic Block Copolymers and Membrane Proteins. *Rev. Mol. Biotechnol.* **2002**, *90*, 17–26.
43. Löwik, D. W. P. M.; Ayres, L.; Smeenk, J. M.; VanHest, J. C. M. Synthesis of Bio-Inspired Hybrid Polymers Using Peptide Synthesis and Protein Engineering. *Adv. Polym. Sci.* **2006**, *202*, 19–52.
44. Feng, S.; Wang, L.; Palo, P.; Liu, X.; Mallapragada, S. K.; Nilsen-Hamilton, M. Integrated Self-Assembly of the Mms6 Magnetosome Protein to Form an Iron-Responsive Structure. *Int. J. Mol. Sci.* **2013**, *14*, 14594–14606.
45. Arakaki, A.; Masuda, F.; Amemiya, Y.; Tanaka, T.; Matsunaga, T. Control of the Morphology and Size of Magnetite Particles with Peptides Mimicking the Mms6 Protein from Magnetotactic Bacteria. *J. Colloid Interface Sci.* **2010**, *343*, 65–70.
46. Amemiya, Y.; Arakaki, A.; Staniland, S. S.; Tanaka, T.; Matsunaga, T. Controlled Formation of Magnetite Crystal by Partial Oxidation of Ferrous Hydroxide in the Presence of Recombinant Magnetotactic Bacterial Protein Mms6. *Biomaterials* **2007**, *28*, 5381–5389.
47. Arakaki, A.; Masuda, F.; Matsunaga, T. Iron Oxide Crystal Formation on a Substrate Modified with the Mms6 Protein from Magnetotactic Bacteria. *Mater. Res. Soc. Symp. P.* **2009**, *1187*, KK03–KK08.
48. Prozorov, T.; Mallapragada, S. K.; Narasimhan, B.; Wang, L.; Palo, P.; Nilsen-Hamilton, M.; Williams, T. J.; Bazylinski, D. A.; Prozorov, R.; Canfield, P. C. Protein-Mediated Synthesis of Uniform Superparamagnetic Magnetite Nanocrystals. *Adv. Funct. Mater.* **2007**, *17*, 951–957.
49. Prozorov, T.; Bazylinski, D. A.; Mallapragada, S. K.; Prozorov, R. Novel Magnetic Nanomaterials Inspired by Magnetotactic Bacteria: Topical Review. *Mater. Sci. Eng. R* **2013**, *74*, 133–172.
50. Bazylinski, D. A. Synthesis of the Bacterial Magnetosome: The Making of a Magnetic Personality. *Int. Microbiol.* **1999**, *2*, 71–80.
51. Bazylinski, D. A.; Frankel, R. B. Magnetosome Formation in Prokaryotes. *Nat. Rev. Microbiol.* **2004**, *2*, 217–230.
52. Bazylinski, D. A.; Schübbe, S. Controlled Biomineralization by and Applications of Magnetotactic Bacteria. In *Advances in Applied Microbiology*; Laskin, A. I.; Sariaslani, S.; Gadd, G. M., Eds.; Academic Press, 2007; Vol. 62, pp 21–62.
53. Bazylinski, D. A.; Williams, T. J.; Lefèvre, C. T.; Trubitsyn, D.; Fang, J.; Beveridge, T. J.; Moskowitz, B. M.; Ward, B.; Schübbe, S.; Dubbels, B. L.; Simpson, B. Magnetovibrio blakemorei, gen. nov. sp. nov., a New Magnetotactic Bacterium (Alphaproteobacteria: Rhodospirillaceae) Isolated from a Salt Marsh. *Int. J. Syst. Evol. Microbiol.* **2013**, *77*, 497–526.
54. Ginet, N.; Pardoux, R.; Adryanczyk, G.; Garcia, D.; Brutesco, C.; Pignol, D. Single-Step Production of a Recyclable Nanobiocatalyst for Organophosphate Pesticides Biodegradation Using Functionalized Bacterial Magnetosomes. *PLoS One* **2011**, *6*, e21442.
55. Arakaki, A.; Webb, J.; Matsunaga, T. A Novel Protein Tightly Bound to Bacterial Magnetic Particles in Magnetospirillum Magneticum Strain AMB-1*. *J. Biol. Chem.* **2003**, *278*, 8745–8750.
56. Prozorov, T.; Palo, P.; Wang, L.; Nilsen-Hamilton, M.; Jones, D.; Orr, D.; Mallapragada, S. K.; Narasimhan, B.; Canfield, P. C.; Prozorov, R. Cobalt Ferrite Nanocrystals: Out-Performing Magnetotactic Bacteria. *ACS Nano* **2007**, *1*, 228–233.
57. Prozorov, T.; Mallapragada, S. K.; Narasimhan, B.; Wang, L. J.; Palo, P.; Nilsen-Hamilton, M.; Williams, T. J.; Bazylinski, D. A.; Prozorov, R.; Canfield, P. C. Protein-Mediated Synthesis of Uniform Superparamagnetic Magnetite Nanocrystals. *Adv. Funct. Mater.* **2007**, *17*, 951–957.
58. Grünberg, K.; Muller, E.-C.; Otto, A.; Reszka, R.; Linder, D.; Kube, M.; Reinhardt, R.; Schuler, D. Biochemical and Proteomic Analysis of the Magnetosome Membrane in Magnetospirillum gryphiswaldense. *Appl. Environ. Microbiol.* **2004**, *70*, 1040–50.
59. Wolff, A.; Frese, K.; Wissbrock, M.; Eckstaedt, K.; Ennen, I.; Hetaba, W.; Loeffler, S.; Regtmeier, A.; Thomas, P.; Sewald, N.; Schattschneider, P.; Huetten, A. Influence of the Synthetic Polypeptide c25-mms6 on Cobalt Ferrite Nanoparticle Formation. *J. Nanopart. Res.* **2012**, *14*, 1161/1–1161/11.
60. Wolff, A.; Mill, N.; Eckstadt, K.; Ennen, I.; Hutten, A.; Hetaba, W.; Wissbrock, M.; Sewald, N.; Loffler, S.; Dreyer, A.; Schattschneider, P. Oriented Attachment Explains Cobalt Ferrite Nanoparticle Growth in Bioinspired Syntheses. *Beilstein J. Nanotechnol.* **2014**, *5*, 210–218.
61. Wang, L.; Prozorov, T.; Palo, P. E.; Liu, X.; Vaknin, D.; Prozorov, R.; Mallapragada, S.; Nilsen-Hamilton, M. Self-Assembly and Biphasic Iron-Binding Characteristics of Mms6, A Bacterial Protein That Promotes the Formation of Superparamagnetic Magnetite Nanoparticles of Uniform Size and Shape. *Biomacromolecules* **2012**, *13*, 98–105.
62. Wang, W.; Bu, W.; Wang, L.; Palo, P. E.; Mallapragada, S.; Nilsen-Hamilton, M.; Vaknin, D. Interfacial Properties and Iron Binding to Bacterial Proteins That Promote the Growth of Magnetite Nanocrystals: X-ray Reflectivity and Surface Spectroscopy Studies. *Langmuir* **2012**, *28*, 4274–4282.
63. Grünberg, K.; Wawer, C.; Tebo, B. M.; Schüler, D. A Large Gene Cluster Encoding Several Magnetosome Proteins is Conserved in Different Species of Magnetotactic Bacteria. *Appl. Environ. Microbiol.* **2001**, *67*, 4573–4582.
64. Schübbe, S.; Williams, T. J.; Xie, G.; Kiss, H. E.; Brettin, T. S.; Martinez, D.; Ross, C. A.; Schüler, D.; Cox, B. L.; Nealson, K. H.; Bazylinski, D. A. Complete Genome Sequence of the Chemolithoautotrophic Marine Magnetotactic Coccus Strain MC-1. *Appl. Environ. Microbiol.* **2009**, *75*, 4835–4852.
65. Tanaka, M.; Okamura, Y.; Arakaki, A.; Tanaka, T.; Takeyama, H.; Matsunaga, T. Origin of Magnetosome Membrane: Proteomic Analysis of Magnetosome Membrane and Comparison with Cytoplasmic Membrane. *Proteomics* **2006**, *6*, 5234–5247.

66. Valverde-Tercedor, C.; Abadía-Molina, F.; Martinez-Bueno, M.; Pineda-Molina, E.; Lower, B. H.; Chen, L.; Oestreicher, Z.; Lower, S. K.; Bazylinski, D. A.; Jimenez-Lopez, C. Subcellular Localization of the Magnetosome Protein MamC in the Marine Magnetotactic Bacterium Magnetococcus Marinus Strain MC-1 Using Immunoelectron Microscopy. *Arch. Microbiol.* **2014**, *196*, 481–488.
67. Kashyap, S.; Woehl, T. J.; Valverde-Tercedor, C.; Sanchez-Quesada, M. S.; Jimenez-Lopez, C.; Prozorov, T. Visualization of Iron-Binding Micelles in Acidic Recombinant Biomineralization Protein, MamC. *J. Nanomater.* **2014**, 320124.
68. Hamaya, T. Magnetotactic Bacteria and *in Vitro* Magnetite Formation. *Superbugs* **1991**, *4*, 54–60.
69. Faivre, D. Biomimetic Formation of Magnetite Nanoparticles. In *Handbook of Biomineralization: Biomimetic and Bioinspired Chemistry*; Schuler, D., Ed.; Wiley, 2007; pp 159−171.
70. Faivre, D.; Menguy, N.; Guyot, F.; Lopez, O.; Zuddas, P. Morphology of Nanomagnetite Crystals: Implications for Formation Conditions. *Am. Mineral.* **2005**, *90*, 1793–1800.
71. Schüler, D. Formation of Magnetosomes in Magnetotactic Bacteria. *J. Mol. Microb. Biotechnol.* **1999**, *1*, 79–86.
72. Schüler, D. Biochemical and Genetic Analysis of the Magnetosome Membrane in Magnetospirillum gryphiswaldense. In *Biomineralization: From Biology to Biotechnology and Medical Application*; Wiley, 2004; pp 61−73.
73. Frankel, R. B.; Bazylinski, D. A. Magnetosomes: Nanoscale Magnetic Iron Minerals in Bacteria. *Nanobiotechnology* **2004**, 136–145.
74. Kawasaki, K.; Buchanan, A. V.; Weiss, K. M. Biomineralization in Humans: Making the Hard Choices in Life. *Annu. Rev. Genet.* **2009**, *43*, 119–142.
75. Brown, S.; Sarikaya, M.; Johnson, E. A Genetic Analysis of Crystal Growth. *J. Mol. Biol.* **2000**, *299*, 725–735.
76. Li, D.; Nielsen, M. H.; Lee, J. R. I.; Frandsen, C.; Banfield, J. F.; De Yoreo, J. J. Direction-Specific Interactions Control Crystal Growth by Oriented Attachment. *Science* **2012**, *336*, 1014–1018.
77. Cha, T.-G.; Baker, B. A.; Salgado, J.; Bates, C. J.; Chen, K. H.; Chang, A. C.; Akatay, M. C.; Han, J.-H.; Strano, M. S.; Choi, J. H. Understanding Oligonucleotide-Templated Nanocrystals: Growth Mechanisms and Surface Properties. *ACS Nano* **2012**, *6*, 8136–8143.
78. Zheng, H.; Smith, R. K.; Jun, Y.-W.; Kisielowski, C.; Dahmen, U.; Alivisatos, A. P. Observation of Single Colloidal Platinum Nanocrystal Growth Trajectories. *Science* **2009**, *324*, 1309–1312.
79. Ring, E. A.; de Jonge, N. Microfluidic System for Transmission Electron Microscopy. *Microsc. Microanal.* **2010**, *16*, 622–629.
80. Grogan, J. M.; Bau, H. H. The Nanoaquarium: A Platform for *in Situ* Transmission Electron Microscopy in Liquid Media. *J. Microelectromech. Syst.* **2010**, *19*, 885–894.
81. Evans, J. E.; Arslan, I.; Browning, N. D.; Campbell, G. H.; Jungjohann, K.; La Grange, T. B.; Mehraeen, S.; Reed, B. W.; Parent, L. R.; Santala, M.; Wall, M. Studying Materials *in Situ* with the Dynamic Transmission Electron Microscope (DTEM). *Microsc. Microanal.* **2010**, *16*, 320–321.
82. Klein, K. L.; Anderson, I. M.; De Jonge, N. Transmission Electron Microscopy with a Liquid Flow Cell. *J. Microsc.* **2011**, *242*, 117–123.
83. Evans, J. E.; Jungjohann, K. L.; Wong, P. C. K.; Chiu, P.-L.; Dutrow, G. H.; Arslan, I.; Browning, N. D. Visualizing Macromolecular Complexes with *in Situ* Liquid Scanning Transmission Electron Microscopy. *Micron* **2012**, *43*, 1085–1090.
84. Colliex, C. Watching Solution Growth of Nanoparticles in Graphene Cells. *Science* **2012**, *336*, 44–45.
85. Wang, C.; Qiao, Q.; Shokuhfar, T.; Klie, R. F. High-Resolution Electron Microscopy and Spectroscopy of Ferritin in Biocompatible Graphene Liquid Cells and Graphene Sandwiches. *Adv. Mater.* **2014**, *26*, 3410−3414.
86. Peckys, D. B.; de Jonge, N. Liquid Scanning Transmission Electron Microscopy: Imaging Protein Complexes in their Native Environment in Whole Eukaryotic Cells. *Microsc. Microanal.* **2014**, 1–20.
87. Parent, L. R.; Robinson, D. B.; Woehl, T. J.; Ristenpart, W. D.; Evans, J. E.; Browning, N. D.; Arslan, I. Direct *in Situ* Observation of Nanoparticle Synthesis in a Liquid Crystal Surfactant Template. *ACS Nano* **2012**, *6*, 3589–3596.
88. Woehl, T. J.; Evans, J. E.; Arslan, I.; Ristenpart, W. D.; Browning, N. D. Direct *in Situ* Determination of the Mechanisms Controlling Nanoparticle Nucleation and Growth. *ACS Nano* **2012**, *6*, 8599–8610.
89. Woehl, T. J.; Park, C.; Evans, J. E.; Arslan, I.; Ristenpart, W. D.; Browning, N. D. Direct Observation of Aggregative Nanoparticle Growth: Kinetic Modeling of the Size Distribution and Growth Rate. *Nano Lett.* **2014**, *14*, 373–378.
90. Mirsaidov, U. M.; Zheng, H. M.; Casana, Y.; Matsudaira, P. Imaging Protein Structure in Water at 2.7 nm Resolution by Transmission Electron Microscopy. *Biophys. J.* **2012**, *102*, L15–L17.
91. Parent, L. R.; Robinson, D. B.; Cappillino, P. J.; Hartnett, R. J.; Abellan, P.; Evans, J. E.; Browning, N. D.; Arslan, I. *In Situ* Observation of Directed Nanoparticle Aggregation during the Synthesis of Ordered Nanoporous Metal in Soft Templates. *Chem. Mater.* **2014**, *26*, 1426–1433.
92. Proetto, M. T.; Rush, A. M.; Chien, M. P.; Baeza, P. A.; Patterson, J. P.; Thompson, M. P.; Olson, N. H.; Moore, C. E.; Rheingold, A. L.; Andolina, C.; Millstone, J.; Howell, S. B.; Browning, N. D.; Evans, J. E.; Gianneschi, N. C. Dynamics of Soft Nanomaterials Captured by Transmission Electron Microscopy in Liquid Water. *J. Am. Chem. Soc.* **2014**, *136*, 1162–1165.
93. White, E. R.; Singer, S. B.; Augustyn, V.; Hubbard, W. A.; Mecklenburg, M.; Dunn, B.; Regan, B. C. *In Situ* Transmission Electron Microscopy of Lead Dendrites and Lead Ions in Aqueous Solution. *ACS Nano* **2012**, *6*, 6308–6317.
94. Sun, M.; Liao, H.-G.; Niu, K.; Zheng, H. Structural and Morphological Evolution of Lead Dendrites during Electrochemical Migration. *Sci. Rep.* **2013**, *3*, 3227.
95. Atkinson, R. J.; Posner, A. M.; Quirk, J. P. Crystal Nucleation and Growth in Hydrolyzing Iron(III) Chloride Solutions. *Clays Clay Mineral. Conf. Proc.* **1977**, *25*, 49–56.
96. Gyani, B. P.; Misra, R. Hydrolysis and Other Changes in Ferric Chloride Solutions. *J. Ind. Chem. Soc.* **1954**, *31*, 499–508.
97. Schneider, W. Hydrolysis of Iron(III) - Chaotic Olation *versus* Nucleation. *Commun. Inorg. Chem.* **1984**, *3*, 205–23.
98. Balt, S. Hydrolysis in Concentrated Aqueous Solutions of Iron Trichloride. *J. Inorg. Nucl. Chem.* **1967**, *29*, 2307–11.
99. Biedermann, G.; Chow, J. T. Hydrolysis of Metal Ions. LVII. Hydrolysis of the Fe(III) Ion and the Solubility Product of the $Fe(OH)_{2.70}Cl_{0.30}$ in 0.5M (Na+)Cl-Medium. *Acta Chem. Scand.* **1966**, *20*, 1376–88.
100. Arakaki, A.; Tanaka, M.; Matsunaga, T. Protein-Mediated Morphological Control of Magnetite Crystal in Magnetotactic Bacteria. *Pacifichem 2010, International Chemical Conference of the Pacific Basin Society, Honolulu, HI, United States, December 15−20, 2010*; **2010**, MATNANO-42.
101. Wang, L.; Nilsen-Hamilton, M. Biomineralization Proteins: from Vertebrates to Bacteria. *Front. Biol.* **2013**, *8*, 234–246.
102. Xu, J.; Lynch, M.; Huff, J. L.; Mosher, C.; Vengasandra, S.; Ding, G.; Henderson, E. Microfabricated Quill-Type Surface Patterning Tools for Creation of Biological Micro/Nano Arrrays. *Biomed. Microdevices* **2004**, *6*, 117–123.
103. Xua, J.; Lynch, M.; Nettikadan, S.; Mosher, C.; Vegasandra, S.; Henderson, E. Microfabricated "Biomolecular Ink Cartridges"—Surface Patterning Tools (SPTs) for the Printing of Multiplexed Biomolecular Arrays. *Sens. Actuators, B* **2006**, 1034–1041.

104. Huang, K.-W.; Hsieh, C.-W.; Kan, H.-C.; Hsieh, M.-L.; Hsieh, S.; Chau, L.-K.; Cheng, T.-E.; Lin, W.-T. Improved Performance of Aminopropylsilatrane over Aminopropyltriethoxysilane as a Linker for Nanoparticle-Based Plasmon Resonance Aensors. *Sens. Actuators, B* **2012**, *163*, 207–215.
105. Huang, A.; Liang, F.; Steinbach, F.; Caro, J. Preparation and Separation Properties of LTA Membranes by Using 3-Aminopropyltriethoxysilane as Covalent Linker. *J. Membr. Sci.* **2010**, *350*, 5–9.